International Journal of Pressure Vessels and Piping 216 (2025) 105527

Contents lists available at ScienceDirect

International Journal of Pressure Vessels and Piping

journal homepage: www.elsevier.com/locate/ijpvp

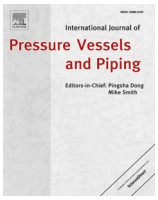

Development of an experimental setup for testing X52 steel SENT specimens in electrolytic hydrogen to explore repurposing potential of pipelines

Flavio Catalano [a,*], Marco Palombo [b], Marco De Marco [b], Michelangelo Mortello [b], Filippo Alberto Recanzone [c], Marcello Baricco [c], Ivan Milano [a], Paolo Piccardo [a], Roberto Spotorno [a]

[a] Department of Chemistry and Industrial Chemistry, University of Genoa, Via Dodecaneso 31, Genoa, 16146, Italy
[b] Istituto Italiano della Saldatura-Ente Morale, Lungobisagno Istria 15A, Genoa, 16141, Italy
[c] Department of Chemistry and NIS Interdepartmental Center, INSTM, University of Turin, Via Pietro Giuria 7, Turin, 10125, Italy

ARTICLE INFO

Keywords:
Hydrogen embrittlement
X52
Non-metallic inclusion
Fracture mechanics
SENT

ABSTRACT

Hydrogen is considered a key alternative to fossil fuels in the broader context of ecological transition. Repurposing natural gas pipelines for hydrogen transport is one of the challenges of this approach. However, hydrogen can diffuse into metallic lattices, leading to hydrogen embrittlement (HE). For this reason, typically ductile materials can experience unexpected brittle fractures, and it is therefore necessary to assess the HE propensity of the current pipeline network to ensure its fitness for hydrogen transport. This study examines the relationship between the microstructure of the circumferential weld joint in X52 pipeline steel and hydrogen concentration, introduced electrolytically. Base material, heat affected zone and fused zone were subjected to 1800, 3600, 7200 and 14400 s of continuous charging with a current density $J = -10$ mA/cm^2 in an acid solution. Results showed that the fusion zone absorbed the most hydrogen across all charging times, while the base material absorbed more hydrogen than the heat-affected zone due to the presence of non-metallic inclusions. Fracture toughness was assessed using single edge notch tension specimens (SENT) in air and electrolytic hydrogen. Results indicate that the base material is particularly vulnerable to hydrogen environments, exhibiting the greatest reduction in toughness when exposed to hydrogen compared to air.

1. Introduction

In recent years, global attention has shifted to sustainable energy solutions to mitigate climate change. International agreements require the progressive abandonment of fossil fuels, responsible for significant greenhouse gas emissions, and promote instead favour clean energy sources [1]. A solution to this challenge is the use of hydrogen, a key energy carrier due to its ability to be stored and transported to meet energy demand (Power-to-Gas principle, P2G [2]). For distances beyond 500 km, gas pipelines represent the most economically and environmentally efficient solution [3]. Europe currently has approximately 200,000 km of gas transport pipelines, over 2 million km of local distribution networks, and more than 20,000 gas pressure regulation stations [4]. Repurposing this network for hydrogen transport is the cheapest and fastest solution [5]. However, a major challenge in this transition is hydrogen embrittlement (HE) [6].

Hydrogen can penetrate in the steel's crystalline lattice, diffused into interstitial sites or trapped in microstructural defects such as grain boundaries, dislocations, vacancies, non-metallic inclusions, and crack-tip zones [7]. This process progressively degrades the material's mechanical properties, increasing the risk of structural failure. Since hydrogen gas forms explosive mixtures with the atmospheric oxygen, a pipeline leak or rupture could have dangerous consequences [8].

The API 5L standard [9] regulates high-strength low-alloy (HSLA) steels used in pipelines, with common grades including X42, X52, X65, and X70 [10]. The European pipeline network exhibits heterogeneity in chemical composition, microstructure, and mechanical properties, not only across different grades, but also within the same grade, depending on production period [11]. Additionally, welded joints represent critical regions, where microstructural changes, residual stresses, and hydrogen

* Corresponding author.
E-mail addresses: flavio.catalano@edu.unige.it, flavio.catalano@iis.it (F. Catalano).

https://doi.org/10.1016/j.ijpvp.2025.105527
Received 17 January 2025; Received in revised form 7 April 2025; Accepted 8 April 2025
Available online 9 April 2025

uptake further compromise material integrity. Studies have shown that medium-strength steels (X42 and X52) exhibit a higher degree of resistance to HE than higher-strength steels (X80 and X100) [12]. Experimental tests on API 5L steels exposed to 100 bar of H_2 indicate that their fracture toughness (K_{Ic}) remains above the ASME B31.12 threshold of 55 MPa$\sqrt{m}$ [13]. However welded zones show increased crack propagation susceptibility, particularly when hardness exceeds 250 HV [13]. API 5L steels can be upgraded to transport hydrogen, but their service life is highly dependent on the design code used and the parameters adopted for crack growth assessment. For a more accurate evaluation, it is advisable to combine specific experimental data with fracture growth curves for the material under consideration [14].

Hydrogen can be introduced into steel via gaseous charging or electrochemical charging. While gaseous charging better replicates real-world operating conditions, electrochemical charging offers other key advantages.

- Higher hydrogen uptake efficiency, enabling faster material assessment. This provides a rapid screening tool: if a material withstands electrochemical charging, it is highly likely to perform well under gaseous hydrogen exposure [15].
- Lower experimental costs and complexity, reducing safety concerns compared to high-pressure gas testing [16].
- Simulates real-world conditions, such as a pipeline in contact with soil under coating failure and cathodic protection scenarios [17].

Although the generation of hydrogen atoms and their absorption in the steel surface differ significantly between the two mechanisms, atomic hydrogen absorption, diffusion through the lattice, and interaction with traps, remain largely similar or even identical for both charging methods [18,19]. However, differences in the activation of diffusible hydrogen traps have been observed between electrochemical and gas-phase charging, primarily due to variations in hydrogen fugacity [20].

During electrochemical charging, it is crucial to use a recombination poison, a substance that prevents hydrogen atoms from recombining into molecular hydrogen (H_2), thereby increasing charging efficiency. The most used poisons are sulfur [21–23] and arsenic compounds [24–26]. The one most widely used in recent years is thiourea, due to its effectiveness, low cost and toxicity [27].

Hydrogen embrittlement (HE) significantly reduces fracture toughness, leading to a transition from ductile to brittle fracture mechanisms [28]. To assess the degradation, fracture mechanics tests are essential. Among these, single-edge notch tension (SENT) specimens have proven to be particularly effective, as their geometry accurately simulates the stress and strain fields at the crack tip, replicating the fracture behaviour observed in pipelines [29–32].

This study analyses the mechanical and microstructural behaviour of the circumferential weld of an API 5L X52 steel pipeline, extracted from a 1970s Italian gas pipeline. A cost-effective experimental setup was developed to perform fracture mechanics tests during electrochemical hydrogen charging. First, optimal conditions were identified to rapidly reach the critical threshold of 1 ppm H, beyond which HE becomes significant in HSLA steels [21]. Finally, the base material (BM), heat-affected zone (HAZ), and fusion zone (FZ) were tested using SENT specimens, both in air and electrochemical hydrogen environments, to assess the effect of hydrogen on fracture toughness.

2. Materials and methods

2.1. Test material and geometry

The material used in the tests is a portion of API 5L X52 steel cut from a 1970s Italian gas pipeline (Fig. 1A). The external diameter of the pipe is 660 mm while the thickness is 12.7 mm. The pipe has two welds: submerged arc welding SAW-longitudinal (Fig. 1B) and shielded metal arc welding SMAW-circumferential (Fig. 1C).

Macrographs show that the longitudinal weld was completed in two passes, while the circumferential welding in four. The composition of the BM and the circumferential weld were analysed using an ARL 3460 OES quantometer, giving the results reported in Table 1.

Some BM samples were treated in an oven for 20 min at 870 °C and then cooled in forced air to simulate HAZ. They were microstructurally and mechanically characterized to verify their similarity to HAZ.

For electrolytic charging tests, BM and HAZ were cut into 1.0 × 0.9 × 1.5 cm^3 cuboids. Cylindrical samples with radius about 8 mm and height 1.3 cm were taken from the FZ.

The SENT specimens had the following dimensions: W (specimen width, measured in the direction of the notch) = 7.8 mm, B (specimen thickness, perpendicular to the width) = 15.6 mm and H (distance between clamped grips) = 78.0 mm with an initial notch produced by EDM having depth 2.0 mm. In addition, there are two 11.0 × 16.0 × 11.0 mm^3 prismatic heads (Fig. 3b). The specimens notched in HAZ and FZ were taken with NQ [33] (notch normal to weld thickness direction) configuration (Fig. 3a). All specimens were cleaned with SiC P1200 sandpaper.

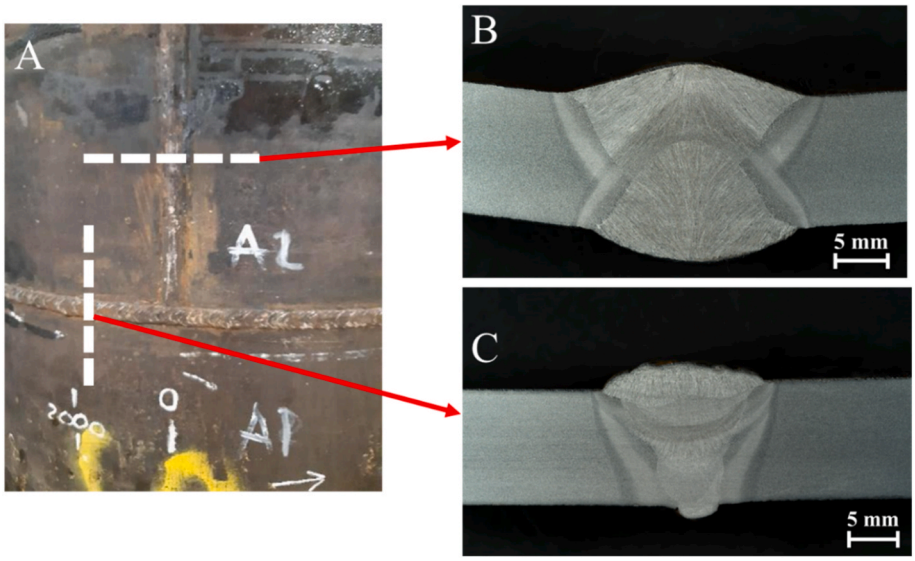

Fig. 1. (a) API 5L X52 pipe. (b) *Macrographs of longitudinal and* (c) *circumferential welding.*

Table 1
Chemical composition, obtained from quantum metric analysis, of the BM and FZ (Fe balance).

Base material composition										
Element	C	Mn	P	S	Si	Cr	No	Nb	Mo	Ti
wt%	0.250	1360	0.011	0.019	0.270	0.023	0.027	0.030	0.004	0.006
Weld metal composition										
Element	C	Mn	P	S	Si	Cr	No	Nb	Mo	Ti
wt%	0.140	0.670	0.011	0.015	0.240	0.020	0.016	0.003	0.428	0.013

2.2. Set-up

Hydrogen charging and fracture mechanics tests were performed in a customized set up. A 12 cm sided cubic cell, open on one face, was assembled from 0.5 cm thick polycarbonate sheets (Fig. 2). Two 12 mm diameter threaded holes were drilled at the bottom of the cell. The first one was made for draining the electrolyte solution, whilst the second one was used for fixing the specimen basement. At the top of the cell the specimen is fixed to the upper grip. From the outside, it is screwed to the crossbar of the Mayes universal testing machine. The grips were fabricated by electrical discharge machining (EDM) of an AISI 314L steel rod and fitted with custom slots for the heads of the SENT specimens used. Charging was carried out by a Gamry Interface 1010E potentiostat which was set in galvanostatic mode with $J = -10$ mA/cm^2 to work with an electrolyte solution consisting of 0.98 g/L H_2SO_4 (0,01 mol/L) and 2.00 g/L CSN_2H_4. The working electrode is the sample (charging specimen or SENT), the counter electrode is a platinum wire spirally wound between polycarbonate rods drilled to surround the specimen. The counter electrode is the standard Ag, AgCl/KCl 3M.

2.3. Procedure

For metallographic analysis, the samples were embedded in resin, then polished with P500 to P1000 SiC papers followed by diamond pastes from 3 to ¼ μm. Subsequently, the samples were etched with 1 % Nital solution (composed of 99 wt% ethanol and 1 wt% nitric acid) and examined using a Zeiss Axio Imager Z2 metallographic optical microscope (LOM) and a Zeiss EVO 15 scanning electron microscope (SEM).

Charging specimens were charged continuously for four fixed times of 1800, 3600, 7200 and 14400 s. To be sure that no chemical alterations could occur due to excessive charging time, the solution was reintroduced every 14400 s, i.e. at the end of the maximum continuous charging time foreseen by the experiment. The standard deviation calculated from the concentration values is shown as the error on the concentration.

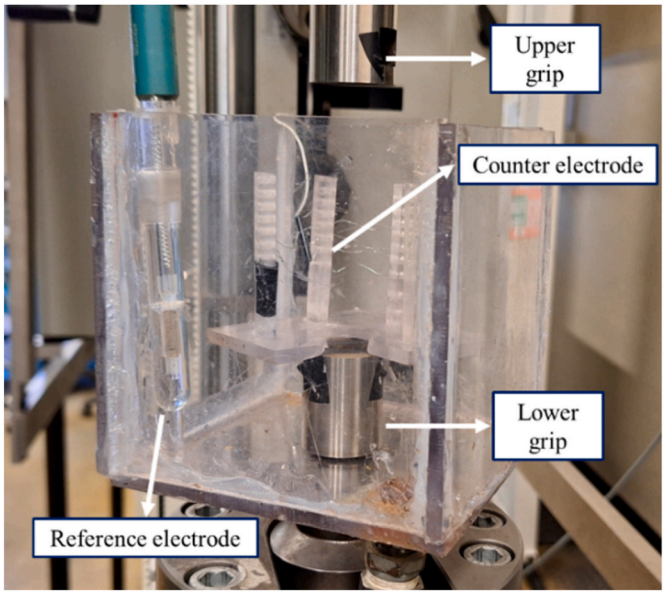

Fig. 2. Electrolytic cell used for hydrogen charging and mechanical testing.

The charging efficiency, i.e. the ratio between the amount of hydrogen absorbed and the amount of hydrogen reduced on the surface of the specimen, is estimated by comparing the measured hydrogen concentration with the theoretical concentration calculated as described in Equation (1) [34]:

$$C_H = \frac{Q_H^{Ev} \cdot MM_H}{zFVd_{steel}} \cdot 10^6 \quad \text{Eq 1}$$

where Q_H^{Ev} is the quantity of electric charge used [A·s], MM_H is the atomic mass of hydrogen [g/mol], z is the number of electrons exchanged, F is the Faraday constant [96485.3365 C/mol], V is the volume of the specimen [cm^3] and d is the density of steel [g/cm^3].

Before measuring the hydrogen concentration, the specimens were treated with ethanol, acetone and ethyl ether. Diffusible hydrogen concentration was determined by placing the specimens in a Phoenix G4 Bruker thermal desorber analyser (DTA) oven for 20 min at 400 °C according with ISO 3690 standard [35].

SENT specimens were fatigue pre-cracked with the Vibrophore 250 Zwick/Roell, to obtain a total defect length (a_0) of about 0.5 W (i.e. 3.7 mm). During the test, the crossbar moves at 0.05 mm/min (K_{rate} = 10 MPa·m^{0,5}/min) until the SENT ruptures. The crack mouth opening displacement (CMOD) during the test was measured with 1-LY41-6/350V3 HBK strain gauges applied to a suitable clip on. The heads of the specimens were electrically insulated with Kapton tape, while the clip-on rods with PVC tape (Fig. 3b). At the end of the test, one of the two parts into which the specimen was broken was used to determinate the hydrogen concentration, the other for fractographic analysis. The value of the integral J was calculated, according with BS 8571 [33] standard, at the maximum load (basic method), as in Equation (2).

$$J = J_{EL} + J_{PL} = \frac{K^2}{E'} + \frac{\eta_p \cdot U_p}{B(W - a_0)} \quad \text{Eq. 2}$$

where J_{EL} is J elastic component [N/mm], J_{PL} is J plastic component [N/mm], K is the stress intensification factor [N/mm$^{1.5}$], E' = E/(1-ν) longitudinal elastic modulus with plane strain [N/mm^2], ν Poisson's coefficient, η_p dimensionless parameter related to geometry, U_p area subtended by the curve F vs. CMOD [N·mm], B specimen thickness [mm], W specimen width [mm], a_0 initial defect length [mm].

3. Results and discussion

3.1. Material characterization

The BM was subjected to tensile testing at room temperature (Table 2). BM, HAZ and FZ were subjected to Charpy V-notch test (at 0 °C with full size 10x10 × 55 mm^3 specimens) and Vickers HV10 hardness test at room temperature (Table 3).

The mechanical test results are consistent with what is expected for this type of material [9].

The microstructure of the BM (Fig. 4a–b) shows the typical grains of

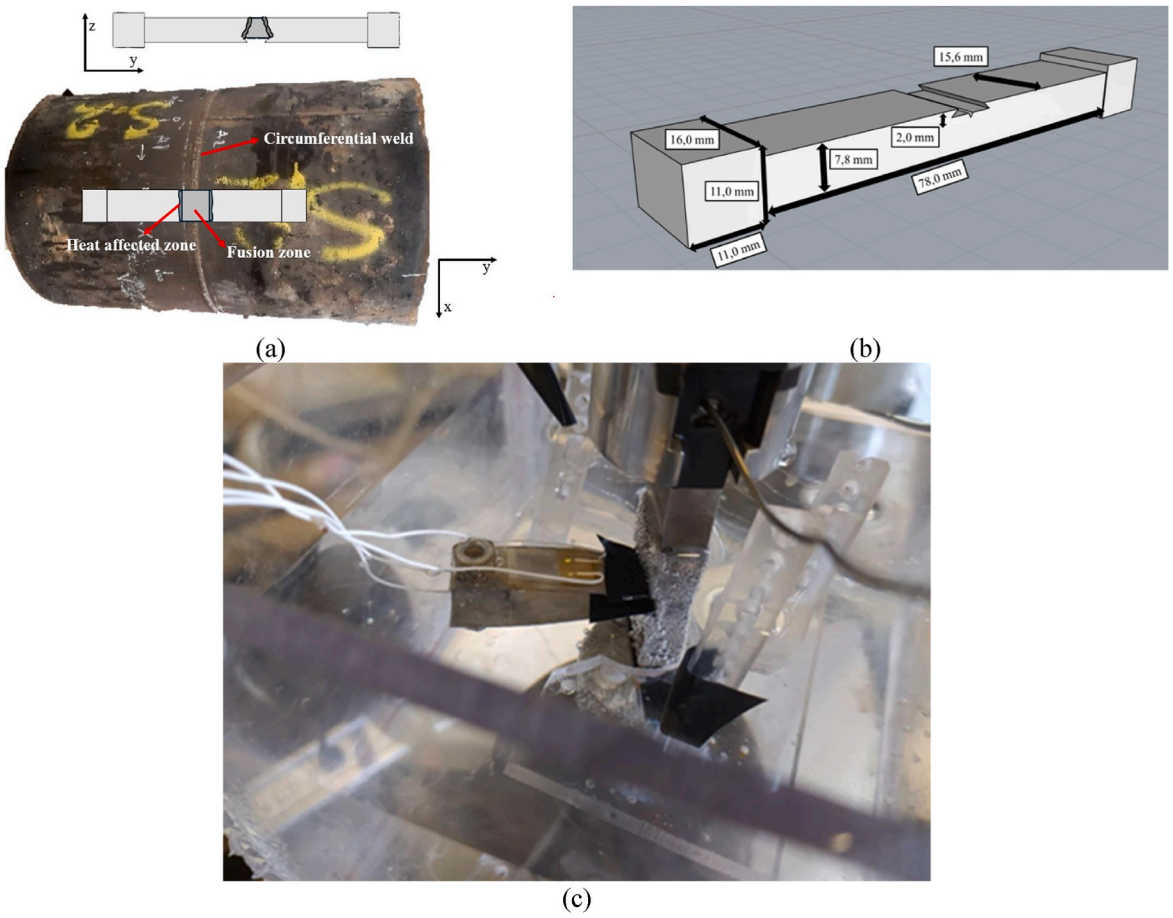

Fig. 3. (a) Front and top view of the SENT specimens extracted from the circumferential pipe weld. (b) Sketch of the SENT specimen. (c) SENT and clip on during the test.

Table 2
Tensile properties of BM tested in air at room temperature.

Elastic modulus [GPa]	$R_{p0,2}$ [MPa]	$R_{t0,5}$ [MPa]	R_m [MPa]	Rupture elongation [%]
207	430	441	605	29

Table 3
Charpy-V impact test and Vickers HV10 test results.

Materials	Absorbed Energy [J]	Hardness HV10
BM	121	199
HAZ	116	206
FZ	50	221

ferrite stretched by the rolling process. The secondary phase is composed of pearlite and mostly very fine carbides, which are probably formed during the hot calendering process undergone by sheet metal. The HAZ has a Widmanstatten-like microstructure composed of ferrite and bainite, with rare pearlite islands (Fig. 4c–d). Welding passes cause a heterogeneous microstructure to the FZ: the lower part annealed by the upper passes took on a ferrite/pearlite conformation (Fig. 4f); the surface is composed of acicular structures (Fig. 4e).

Characterization of the circumferential weld bead also revealed the presence of numerous elongated inclusions in the BM (Fig. 5a) and globular in the FZ (Fig. 5b). The appearance of the inclusions in the BM was compared with the reference pictures in UNI 3244 [36]. SEM-EDXS analysis confirmed the presence of oxides, sulfides and silicates.

The heat-treated BM (reproduced HAZ) was subjected to microstructural (Fig. 6) and mechanical analysis (Table 4).

The heat-treated BM exhibited a microstructure closely analogous to original HAZ's one, characterized by fine ferrite grains interspersed with bainite and pearlite. Hardness, grain size and phase percentage are very similar to the original HAZ. This method provided a viable solution to the extraction challenges, allowing the necessary tests to determine the behaviour of hydrogen in different zones of the weld bead.

3.2. Electrolytic hydrogen charging test

The results obtained for the three types of material are represented in Fig. 7. All three materials have shown to be sensitive to hydrogenation in selected charging conditions. A certain dispersion of data is imputable to.

- non-deaerated solution. Oxygen competes with hydrogen in the reduction process, thus lowering the yield of the hydrogen reduction reaction (HER) [40,41].
- non-constant distance of the specimens from the electrodes. The electrical resistance of the solution varies with the distance between the electrodes and the samples. If a sample is further away, it may experience higher resistance, reducing the efficiency of the applied current and thus the rate of hydrogen evolution [42].
- complex chemical equilibria that develops on the metal-solution interface. In acid solution, hydrogen is reduced and absorbed through a series of chemical equilibria described by the Volmer, Tafel and Heyrovsky equations [17].

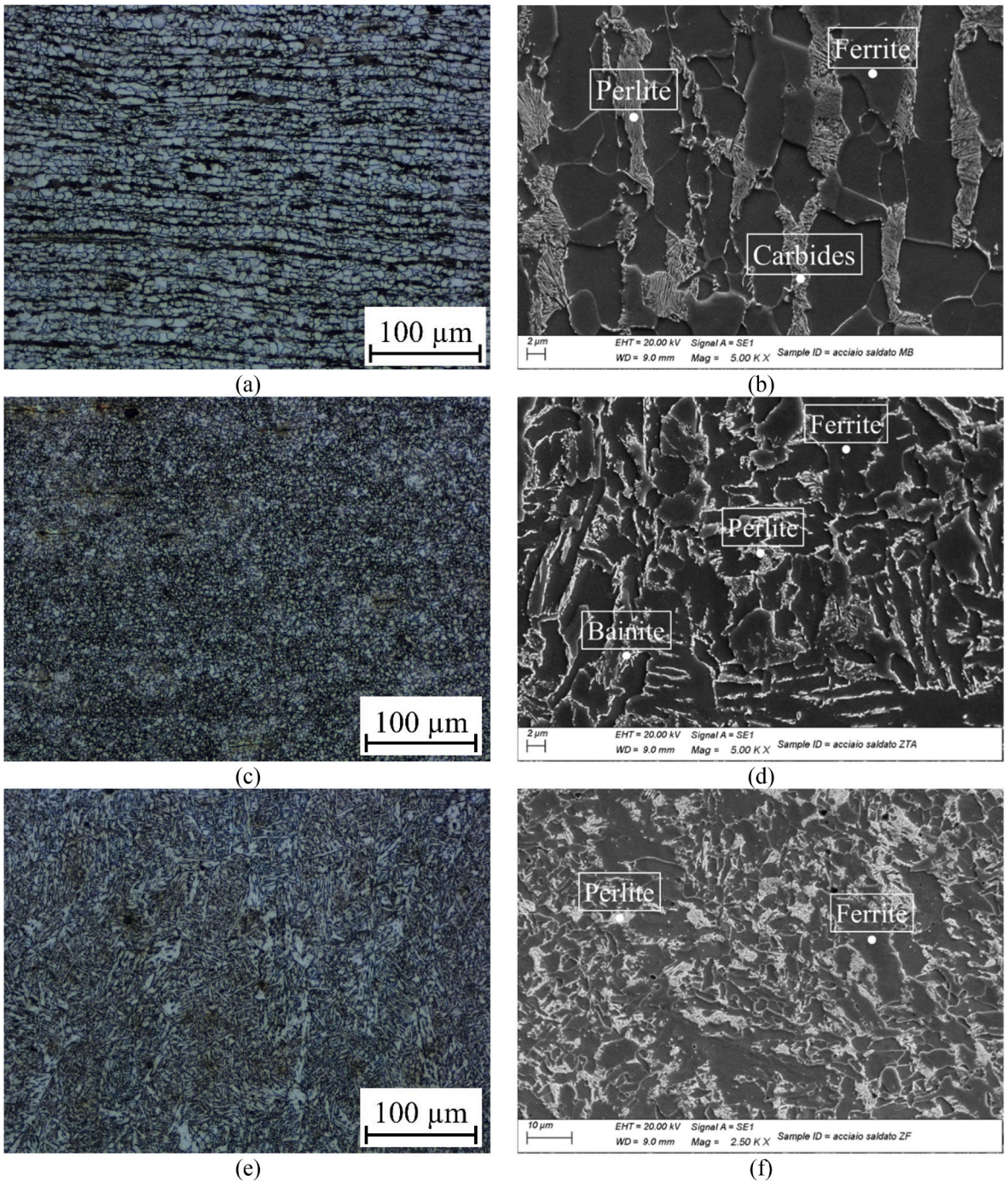

Fig. 4. Weld bead micrographs: (a) BM LOM 200X; (b) BM SEM 5000X; (c) HAZ LOM 200X; (d) HAZ SEM 5000X; (e) FZ LOM 200X; (f) FZ SEM 2500X.

- time elapsed between taking the sample and starting the TDA. In fact, hydrogen concentrations are very low, and hydrogen diffuses quickly in the ferrite [43].

Charging yields were calculated with Eq. (1). For example, a BM specimen is chosen, held under a J of 0.01 A/cm^2 for 3600 s, with A = 7.27 cm^2 and V = 1.25 cm^3, $d_{Steel\ X52}$ = 7.87 g/cm^3. The TDA analysis detected a concentration of 1.24 ppm of hydrogen. The theoretical concentration of hydrogen can be calculated as follows:

$$C_H = \frac{Q_H^{Ev} \cdot MM_H}{zFVd_{Steel}} \cdot 10^6 = \frac{0.01\ \frac{A}{cm^2} \cdot 3600\ s \cdot 7.27\ cm^2 \cdot 1\ \frac{g}{mol}}{1 \cdot 96485.3365\ \frac{C}{mol} \cdot 1.25\ cm^3 \cdot 7.87\ \frac{g}{cm^3}} \cdot 10^6 = 275.73\ ppm$$

which are equivalent to a yield of 0.45 %. The hydrogen absorption efficiency is summarized in Table 5.

The typical trend of hydrogen charging in a steel is a curve that grows until reaching a plateau, when saturation conditions are reached [25,44,45]. Specifically, the three curves show an increasing trend culminating in the maximum value of hydrogen concentration for t = 14400 s. It is interesting to note that for the BM it was possible to charge approximately 1 ppm of H/h [11]. The greater amount of hydrogen charged by the FZ was expected, as this is caused by the finer microstructure, the high concentration of dislocations and the residual stresses that are typical of the welding process. However, fine structures, such as bainite or acicular ferrite, are less sensitive to HE, as they act as irreversible traps, slowing down the motion of hydrogen [46]. Similarly, one would

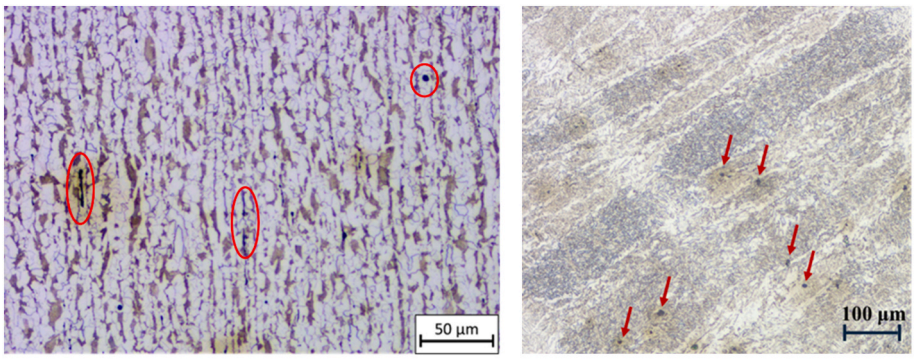

(a) (b)

Fig. 5. (a) inclusions in the BM; (b) globular inclusions in the FZ.

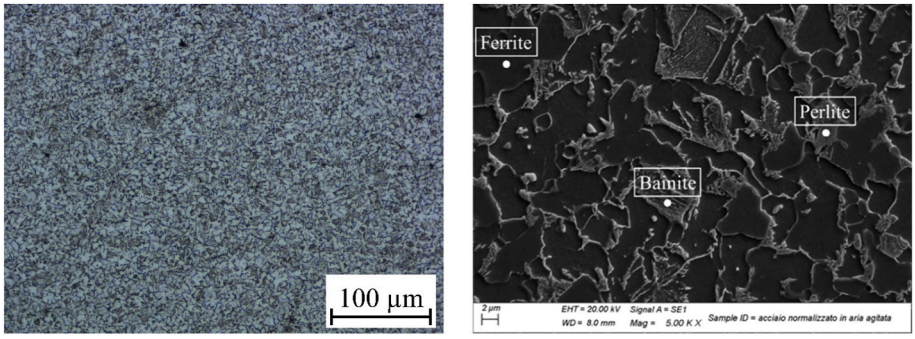

(a) (b)

Fig. 6. Reproduced HAZ micrographs. (a) LOM 200X; (b) SEM 5000X.

Table 4
Comparison of hardness, grain size and phase percentage test results between the original and reproduced HAZ.

Material	Original HAZ	Reproduced HAZ
Hardness HV10 [V]	206.9 ± 10.7	190.5 ± 7.3
ASTM grain size number [37]	13.4 ± 0.9	13.0 ± 0.5
Secondary phase percentage ASTM E562 [38]	23.87 ± 3.93	23.73 ± 4.26
Secondary phase percentage ASTM E1245 [39]	21.66 ± 1.92	19.43 ± 1.95

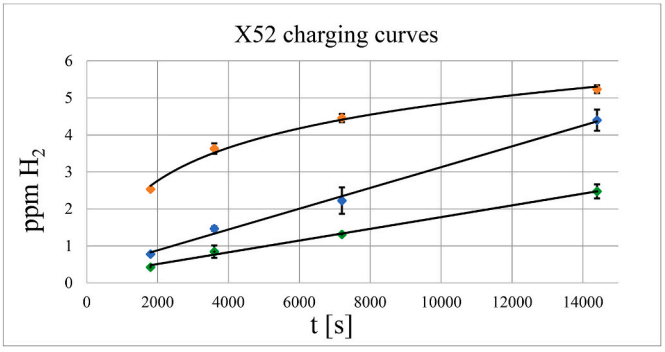

Fig. 7. Electrolytic hydrogen charging curves on BM (blue), HAZ (green) and FZ (orange).

Table 5
Hydrogen charging yields on the specimens tested in this work.

	t [s]	Yield %
BM	1800	0.63
	3600	0.53
	7200	0.43
	14400	0.37
HAZ	1800	0.31
	3600	0.32
	7200	0.25
	14400	0.25
FZ	1800	1.61
	3600	1.17
	7200	0.72
	14400	0.42

expect that the HAZ could store more hydrogen than the BM, but this did not happen. The explanation is to be found in the microstructure of the BM.

The morphology of the inclusions is fundamental in the development of the HE, it is more accentuated when they have an elongated shape (created by the rolling process). This is because hydrogen atoms tend to concentrate more at the end of the inclusions, where the stress concentration is usually higher [47]. Furthermore, for the same mass, an elongated inclusion has a greater surface area than a globular one and therefore more preferential storage sites for hydrogen. Generally, a low concentration of elongated inclusions is more critical than a high concentration of rounded inclusions, as described by the stress concentration theory [48]. Under charging conditions, these elongated inclusions

are susceptible to the accumulation of hydrogen at the interface, and produce cracking, which in turn attracts even greater quantities of hydrogen. This phenomenon creates stress concentration at the crack tip, and from there it diffuses along the rolling direction. The grains of the HAZ, however, underwent a normalization process: they entered the γ field and cooled quickly. The thermal treatment refined the grains and caused them to lose the orientation given by the lamination. Therefore, with the same number of phases (ferrite and pearlite), the HAZ can store less hydrogen than the BM, because the grains and inclusions aren't elongated and oriented in one direction.

Three BM specimens were also tested in the same conditions, but for 18000 s. The observed average hydrogen concentration was 2.43 ppm. As already reported [24,25], after a certain charging period, the hydrogen concentration drops due to the high number of bubbles that form on the surface of the sample. They have a dual effect: first they improve the resistance of the steel (in fact the surface potential gradually increases during the test) and then they hinder the introduction of more hydrogen into the crystalline lattice. Regarding charging yields, calculations show that even under improved setup conditions, almost all the hydrogen produced recombines into a molecule and leaves the electrolytic cell. The rate of entry depends on many variables: the nature of the metal, its composition and thermomechanical history, the surface conditions, the composition of the electrolyte, the cathode current density, the electrode potential, the temperature, the pressure, the concentration and chemical nature of the recombination inhibitor, and the saturation of subsurface layers. As shown in Table 5, as time increases the charging yield decreases, since in all solutions, when the quantity of dissolved solute increases, it becomes increasingly difficult to solubilize.

3.3. Fracture mechanics test with SENT specimens

Force vs. CMOD curves of the specimens tested in air and under electrolyte charging are shown in Fig. 8. The maximum values of the J-integral calculated according to Eq. (2) are shown in Table 6. The J_{MAX} H/J_{MAX} Air ratio was used as an index of embrittlement due to hydrogen charging. The charging conditions tested in the previous experiment resulted in such a high concentration of hydrogen in the test time (about 5400 s) that the critical limit of 1 ppm was exceeded.

The Force vs. CMOD curves show that the hydrogen-charged specimens reach the maximum value sooner, but also reach failure sooner, compared to those tested in air (i.e. have a lower final CMOD). Although BM has higher toughness in air, it is more affected by the hydrogen charging (Table 6). As pointed out in Section 3.2, elongated inclusions play a key role in the process of hydrogen absorption and crack formation [48]. In air, the ferrite and perlite microstructure of BM appeared as more tough than weld metal and HAZ microstructures composed by acicular ferrite and carbides. The behaviour in H is different; therefore, a lower decrease of the toughness (see J values in Table 6) was recorded on HAZ and FZ specimens. They have a lower

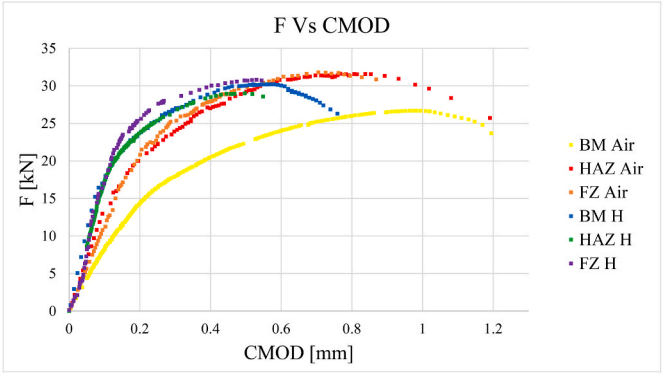

Fig. 8. Force vs CMOD curves for the SENT specimens tested.

Table 6
Values of J_{MAX} calculated for the SENT specimens tested.

Specimen	$J_{MAX\ Air}$ [kJ/m^2]	$J_{MAX\ H}$ [kJ/m^2]	$J_{MAX\ H}/J_{MAX\ Air}$	H concentration [ppm]
BM	1233	727	0.590	1.20
HAZ	1094	751	0.686	1.08
FZ	1032	713	0.690	1.19

tendency to stress concentration and offer greater resistance to hydrogen diffusion. As a result, even when exposed to the same charging conditions and aggressive environment, these zones show greater tolerance to hydrogen embrittlement than the base material. The significant reduction in fracture toughness observed in hydrogen environments is due to hydrogen accumulation at the crack tip in SENT specimens, that weakens plasticity and lowers the stress and energy needed for crack initiation and propagation. The J_{MAX} values obtained are comparable with those obtained in previous experiments [49–51].

In this experiment, the J_{MAX} value fell by 40 % for BM and 30 % for HAZ and FZ. Research has shown that the fracture toughness decreases as the cathodic current used increases [5,52,53]. In fact, other studies have obtained similar results using gaseous charging. Pipeline steels tend to suffer a loss of fracture toughness of 40–60 % in gaseous hydrogen [54]. An X52 tested with 40 bar H_2 experienced a 40.9 % drop in J [55], an X70 50 % in 100 bar H_2 [56], X42 46 % in 65 bar H_2 [57].

3.4. SENT fractography

The fracture surfaces of the uncharged and hydrogen-charged specimens are shown in Fig. 9. The overview of the fracture is reported in Fig. 9a while the SEM Micrographs are shown from Fig. 9b–f. The fatigue pre-crack is observed at the bottom (Fig. 9b). Following this, a narrow band of stable propagation is present, leading into the fracture zone characterized by rapid failure (Fig. 9a). At high magnification, we can identify typical dimples associated with ductile fracture (Fig. 9c), some of which have nucleated around silicon oxide particles (Fig. 9d). In specimens subjected to hydrogen testing, a distinct fracture surface is evident between the fatigue surface and the ductile fracture surface. This region exhibits typical river-like patterns indicative of cleavage fractures, a phenomenon associated with hydrogen embrittlement (Fig. 9e and f).

3.5. SENT longitudinal micrograph

Longitudinal micrographs were observed at LOM (Fig. 10). In general, three zones can be identified: fatigue propagation, stable propagation and the unstable crack propagation. The first is marked by a linear profile, the second by an irregular profile with plastic deformation, and, finally, the third by a straight profile linked to the final rupture. In the stable propagation zone, there are the nucleation sites of microvoids from inclusions (mainly of MnS). In a hydrogen environment, the final rupture exhibits a 45-degree angle and affects a significant portion of the material (Fig. 10e). In contrast, the rupture area and angle are smaller in air (Fig. 10d), so the final failure in air occurs at a slower rate.

4. Conclusions

The following conclusions were obtained from the results presented.

- The experimental setup to perform fracture toughness tests on SENT specimens in electrolytic hydrogen environments was built.
- The optimal charging conditions for reproducibility and amount of hydrogen introduced into the material in static condition were found and confirmed.

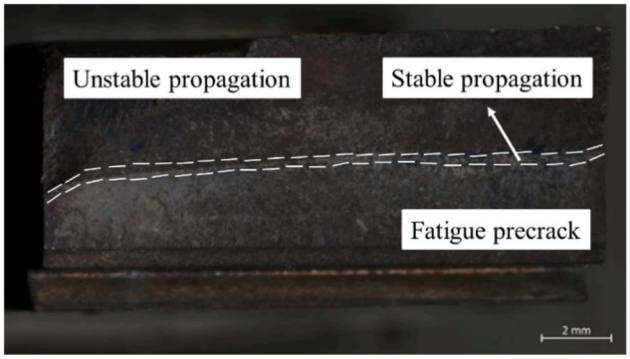

(a)

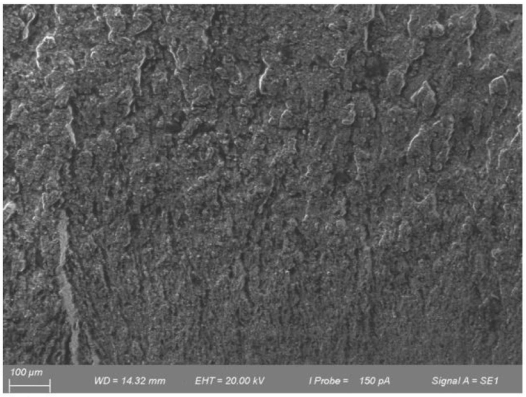

(b)

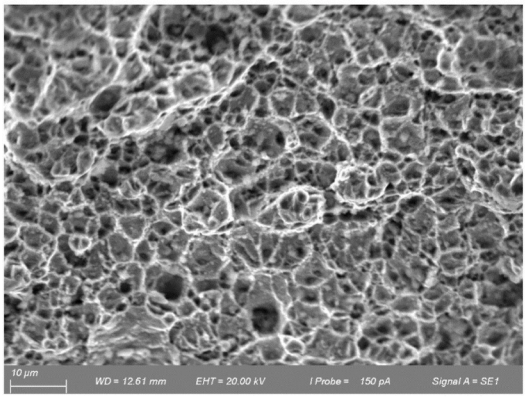

(c)

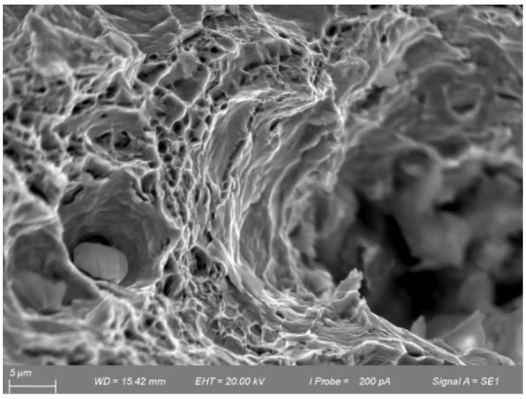

(d)

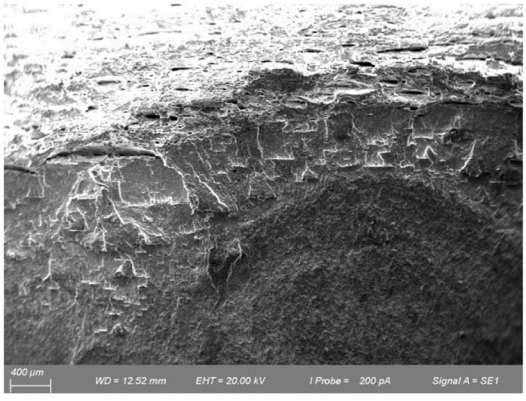

(e)

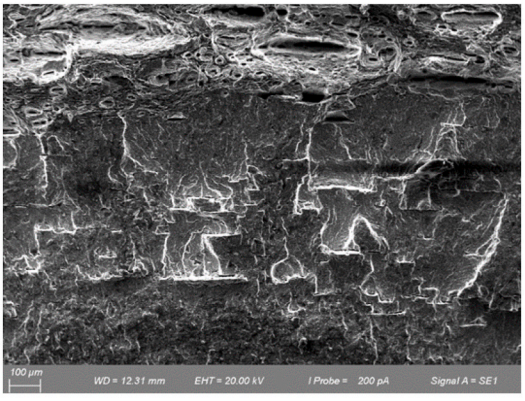

(f)

Fig. 9. (a) Image recorded at 5X with stereographic microscope in which the three different zones of the billing surface (BM) were have been highlighted. (b) Fatigue enhanced zone (BM). (c) Dimples in the stable propagation part (SENT with notch in FZ). (d) Microvacuum accreted around silicon oxide particles. (e) SENT with notch in HAZ charged with H. A brittle fracture section can be seen between the fatigue precrack zone and ductile fracture zone. (f) Cleavage planes in the stable propagation zone of a HAZ-notched SENT.

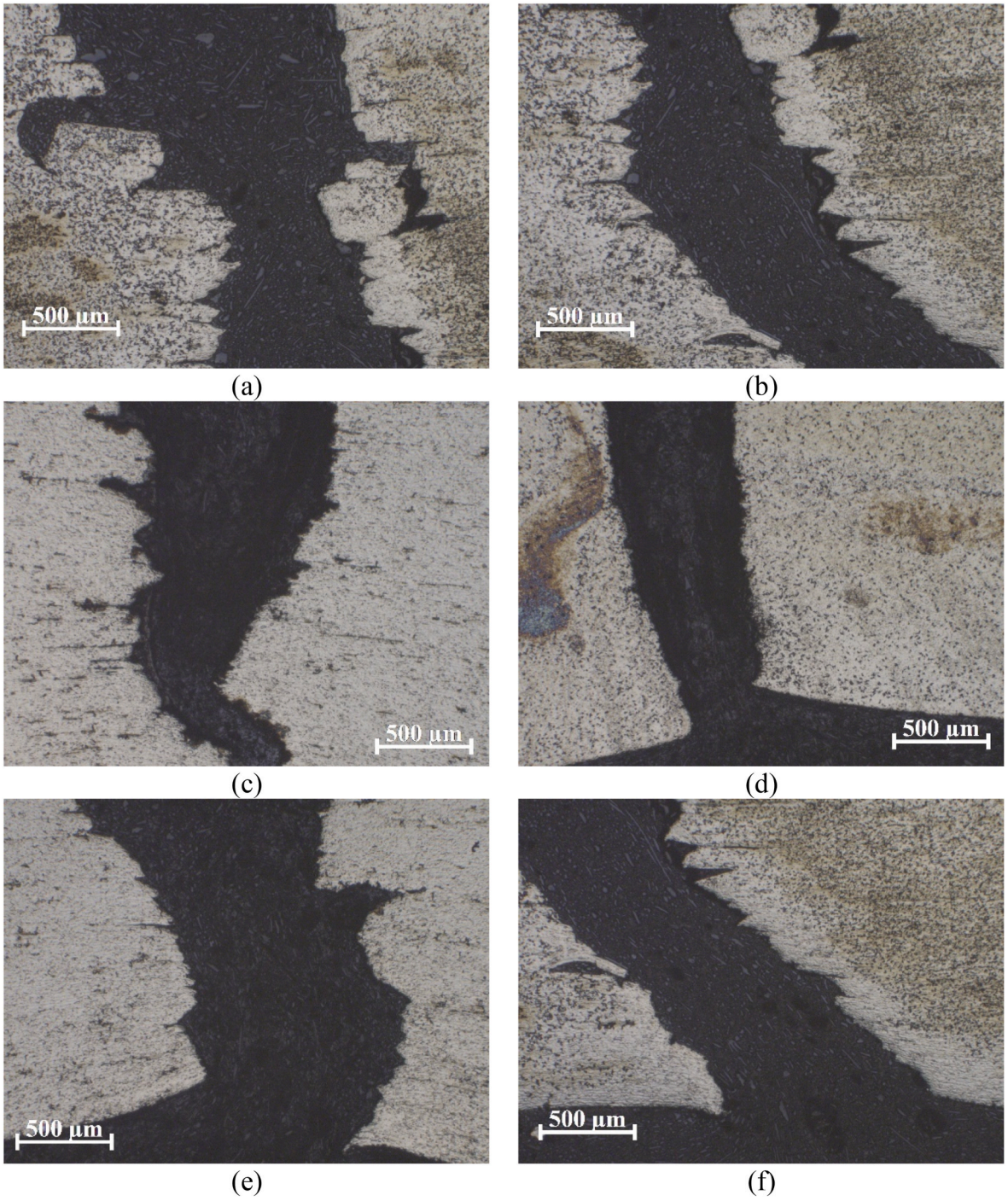

Fig. 10. (a) Transition between fatigue pre-crack and stable propagation in a HAZ specimen charged with H. (b) Transition between stable and unstable propagation zone of the previous specimen. (c) Overall view of the three zones in a BM specimen charged with H. (d) Crash failure zone of a ZF specimen tested in air, (e) HAZ in air and (f) HAZ in H.

- A study of the effect of hydrogen charging time was made and correlated with the microstructure of BM, HAZ and FZ. The tests revealed that, up to 14400 s total charging time, about 1 ppm H/h can be introduced into the BM. The material that absorbs the most hydrogen is FZ, followed by BM and HAZ. The characteristic microstructure of the base material allows it to absorb significantly more hydrogen than anticipated.
- The calculated hydrogen charging results indicate that, as the charging time increases, progressively less hydrogen can penetrate the metal. This can be attributed to two factors: 1) reaching saturation conditions; 2) excessive gas bubble formation that prevents hydrogen atoms from interacting with the metal.
- The hydrogen susceptibility of the weld bead appeared lower than that of the BM; in fact, the J_{MAX} results obtained with the SENT specimens show that the BM has the highest drop in toughness between the tests in air and in hydrogen. Although the FZ has a lower toughness than the BM in air, it was able to absorb a greater amount of hydrogen, with a less detrimental effect on its toughness when tested in hydrogen environment. This suggests that, although the FZ is harder and typically more brittle, its microstructure can better trap

hydrogen, limiting its diffusion and mitigating the HE impact. Interestingly, despite the differences in microstructure and hydrogen uptake between the FZ, BM and HAZ, the J values measured in hydrogen were similar for all the specimens tested, around 700 kJ/m^2. This indicates that, while areas of the material behave differently in air, the presence of hydrogen tends to uniformise their toughness behaviour.

- The effect of hydrogen was investigated through micrographic examination. In fact, a band of cleavage planes can be observed on the fracture surfaces of the charged samples, attributable to a brittle fracture mechanism. On the longitudinally cut fracture surfaces, a sharp deviation of 45° is observed in the final part of the fracture, while for the uncharged samples the fracture continues linearly.
- Considering the high hydrogen content introduced into the material (up to 1 ppm) and the corresponding measured toughness (over ASME limit), it can be concluded that the examined vintage steel shows reasonable compatibility with HE at pressures of 60/80 bar, typical of hydrogen transport applications [58]. These results suggest that the material is suitable for further and more thorough characterization in hydrogen gaseous environment to confirm its fitness for hydrogen service.

CRediT authorship contribution statement

Flavio Catalano: Writing – original draft, Methodology, Investigation, Data curation. **Marco Palombo:** Writing – review & editing, Methodology, Data curation, Conceptualization. **Marco De Marco:** Supervision, Conceptualization. **Michelangelo Mortello:** Writing – review & editing, Funding acquisition. **Filippo Alberto Recanzone:** Investigation. **Marcello Baricco:** Writing – review & editing. **Ivan Milano:** Investigation, Data curation. **Paolo Piccardo:** Supervision, Methodology. **Roberto Spotorno:** Writing – review & editing, Supervision, Methodology.

Declaration of competing interest

The authors declare that they have no known competing financial interests or personal relationships that could have appeared to influence the work reported in this paper.

Acknowledgements

The authors would like to thank Giulia Balbi for her assistance with the English language editing and Fabrizio Catalano for designing the 3D model of the SENT specimen.

Data availability

Data will be made available on request.

References

[1] https://unfccc.int/process-and-meetings/the-paris-agreement [accessed August 2024].
[2] M. Gotz, J. Lefebvre, F. Mors, A. McDaniel Koch, F. Graf, S. Bajohr, R. Reimert, T. Kolb, Renewable Power-to-Gas: a technological and economic review, Renew. Energy 85 (2016) 1371–1390, https://doi.org/10.1016/j.renene.2015.07.066.
[3] IEA. The Future of hydrogen, Seizing Today's Opportunities, Int Energy Agency, 2019. https://www.iea.org/reports/the-future-of-hydrogen. September 2024.
[4] ACER European Union Agency for the Cooperation of Energy Regulators Gas factsheet https://www.acer.europa.eu/gas-factsheet [accessed September 2024].
[5] E.V. Chatzidouros, V.J. Papazoglou, T.E. Tsiourva, D.I. Pantelis, Hydrogen effect on fracture toughness of pipeline steel welds, with in situ hydrogen charging, Int. J. Hydrogen Energy 36 (2011) 12626–12643, https://doi.org/10.1016/j.ijhydene.2011.06.140.
[6] M. Nagumo, Fundamentals of Hydrogen Embrittlement, first ed., Springer, 2016.
[7] G.M. Pressouyre, A classification of hydrogen traps in steel, Mater. Trans. A10 (1979) 1571–1573, https://doi.org/10.1007/BF02812023.
[8] D.A. Crowl, Y. Jo, The hazard and risks of hydrogen, J. Loss Prev. Process. Ind. 20 (2007) 158–164, https://doi.org/10.1016/j.jlp.2007.02.002.
[9] American Petroleum Institute, API Specification 5L - Line Pipe, 2018, p. 46.
[10] S.K. Sharma, Maheshwari. A review on welding of high strength oil and gas pipeline steels, J. Nat. Gas Sci. Eng. 38 (2017) 203–217.
[11] A. Laureys, R. Depraetere, M. Cauwels, T. Depover, S. Hertelè, K. Verbeken, Use of existing steel pipeline infrastructure for gaseous hydrogen storage and transport: a review of factors affecting hydrogen induced degradation, J. Nat. Gas Sci. Eng. 101 (2022) 104534, https://doi.org/10.1016/j.jngse.2022.104534.
[12] H. Wang, Z. Tong, G. Zhou, G. Zhang, H. Zhou, Y. Wang, W. Zheng, Research and Demonstration on Hydrogen Compatibility of Pipelines: a Review of Current Status and Challenges, vol. 66, 2022, pp. 28585–28604, https://doi.org/10.1016/j.ijhydene.2022.06.158.
[13] Steiner M, Marewski U, Silcher H. DVGW Project SyWeSt H2: "Investigation of Steel Materials for Gas Pipelines And Plants for Assessment of their Suitability with Hydrogen". https://www.dvgw.de/medien/dvgw/forschung/berichte/g202006-sywesth2-steel-dvgw.pdf.
[14] H. Oesterlin, C. Fischer, T. Michler, Evaluation of lifetime predictions for future hydrogen pipelines by different fracture mechanics-based design codes, Energy Technol. 13 (2025) 2301012, https://doi.org/10.1002/ente.202301012.
[15] S. Rahimi, K. Verbeken, T. Depover, E. Proverbio, Hydrogen embrittlement of pipeline steels under gaseous and electrochemical charging: a comparative review on tensile properties, Eng. Fail. Anal. 167 (2025) 108956, https://doi.org/10.1016/j.engfailanal.2024.108956.
[16] G. Bai, Q. Wang, Y. Song, H. Deng, D. Li, Y. Li, Study on hydrogen resistance of X42 pipeline steel under electrochemical hydrogen charging condition, in: Proceedings of the. Volume 6: Materials and Fabrication. Virtual, ASME, 2020 V006T06A086, https://doi.org/10.1115/PVP2020-21229. Online. August 3.
[17] A. Lasia, Mechanism and kinetics of the hydrogen evolution reaction, Int. J. Hydrogen Energy 44 (2019) 19484–19518, https://doi.org/10.1016/j.ijhydene.2019.05.183.
[18] T.A. Jack, F. Fazeli, J. Szpunar, Thermal desorption analysis of hydrogen uptake in pipeline steels after gaseous and electrochemical charging, J. Mater. Sci. 60 (2025) 2580–2606, https://doi.org/10.1007/s10853-024-10571-1.
[19] Q. Liu, A.D. Atrens, Z. Shi, K. Verbeken, A. Atrens, Determination of the hydrogen fugacity during electrolytic charging of steel, Corros. Sci. 87 (2014) 239–258, https://doi.org/10.1016/j.corsci.2014.06.033.
[20] J. Venezuela, C. Tapia-Bastidas, Q. Zhou, T. Depover, K. Verbeken, E. Gray, Q. Liu, Q. Liu, M. Zhang, A. Atrens, Determination of the equivalent hydrogen fugacity during electrochemical charging of 3.5NiCrMoV steel, Corros. Sci. 132 (2018) 90–106, https://doi.org/10.1016/j.corsci.2017.12.018.
[21] J. Kittel, J.W. Martin, T. Cassagne, C. Bosch, Hydrogen induced cracking (HIC) - laboratory testing assessment of low alloy steel linepipe, Corrosion (2008).
[22] L. Zhang, H. Shen, K. Lu, W. Cao, Y. Sun, Y. Fang, Y. Xing, Y. Du, M. Lu, Investigation of hydrogen concentration and hydrogen damage on API X80 steel surface under cathodic overprotection, Int. J. Hydrogen Energy 42 (2017) 29888–29896, https://doi.org/10.1016/j.ijhydene.2017.10.116.
[23] T. Depover, D. Pérez Escobar, E. Wallaert, Z. Zermout, K. Verbeken, Effect of Hydrogen Charging on the Mechanical Properties of Advanced High Strength Steels, vol. 39, 2014, pp. 4647–4656, https://doi.org/10.1016/j.ijhydene.2013.12.190.
[24] X.C. Ren, Q.J. Zhou, W.Y. Chu, J.X. Li, Y.J. Su, L.G. Qiao, The mechanism of nucleation of hydrogen blister in metals, Metall. Mater. Trans. 39 (2008) 87–97, https://doi.org/10.1007/s11661-007-9391-3.
[25] P. Rozenak, Hemispherical bubbles growth on electrochemically charged aluminum with hydrogen, Int. J. Hydrogen Energy 32 (2007) 2816–2823, https://doi.org/10.1016/j.ijhydene.2007.01.009.
[26] C.F. Dong, Y.Z. Liu, X.G. Li, Y.F. Cheng, Effects of hydrogen-charging on the susceptibility of X100 pipeline steel to hydrogen-induced cracking, Int. J. Hydrogen Energy 34 (2009) 9879–9884, https://doi.org/10.1016/j.ijhydene.2009.09.090.
[27] B. Yazici, B. Arslan, M. Erbil, S. Zor, Effect of thiourea on the hydrogen yield in electrolysis, Int. J. Hydrogen Energy 23 (1998) 867–872, https://doi.org/10.1016/S0360-3199(97)00142-0.
[28] J.J. Hoyos, M. Masoumi, V.F. Pereira, A.P. Tschiptschin, M.T.P. Paes, J.A. Avila, Influence of hydrogen on the microstructure and fracture toughness of friction stir welded plates of API 5L X80 pipeline steel, Int. J. Hydrogen Energy 44 (2019) 23458–23471, https://doi.org/10.1016/j.ijhydene.2019.06.210.
[29] S. Cravero, C. Ruggieri, Correlation of fracture behavior in high pressure pipelines with axial defects using constraint designed test specimens—Part I: plane-strain analyses, Eng. Fract. Mech. 72 (2005) 1344–1360, https://doi.org/10.1016/j.engfracmech.2004.10.010.
[30] L.A.L. Silva, S. Cravero, C. Ruggieri, Correlation of fracture behavior in high pressure pipelines with axial defects using constraint designed test specimens. Part II: 3-D effects on constraints, Eng. Fract. Mech. 73 (2006) 2123–2138, https://doi.org/10.1016/j.engfracmech.2006.04.004.
[31] M. Dadfarnia, P. Sofronis, B.P. Somerday, D.K. Balch, P. Schembri, R. Melcher, On the environmental similarity for fracture in the SENT specimen and a cracked hydrogen gas pipeline, Eng. Fract. Mech. 78 (2011) 2429–2438, https://doi.org/10.1016/j.engfracmech.2011.06.002.
[32] C. Soret, Y. Madi, J. Besson, V. Gaffard, Use of the Sent Specimen in Pipeline Design, vol. 34, 20th JTM - EPRG European pipeline research group, Paris, France, May 2015 ffhal01183303f. https://minesparis-psl.hal.science/hal01183303/document#:~:text=On%20the%20other%20hand%2C%20the,pressure%20and%20tensile%2C%20or%20bending. March 2024.
[33] BS 8571:2018 Method of Test for Determination of Fracture Toughness in Metallic Materials Using Single Edge Notched Tension (SENT) Specimens.

[34] J. Capelle, I. Dmytrakh, Z. Azari, G. Pluvinage, Evaluation of electrochemical hydrogen absorption in welded pipe, Proc. Mater. Sci. 3 (2014) 550–555, https://doi.org/10.1016/j.ijhydene.2013.08.118.
[35] ISO 3690, Welding and Allied Processes Determination of Hydrogen Content in Arc Weld Metal, 2018.
[36] UNI 3244, Microscopic Examination of Ferrous Materials. Rating of Non-metallic Inclusions in Steels by Reference Pictures, 1980.
[37] ASTM E112-13 Standard Test Methods for Determining Average Grain Size.
[38] ASTM E562-19e1 Standard Test Method for Determining Volume Fraction by Systematic Manual Point Count.
[39] ASTM E1245-03 Standard Practice for Determining the Inclusion or Second-phase Constituent Content of Metals by Automatic Image Analysis.
[40] P. Zhang, M. Laleh, A.K. W, E. Hughes, R. Marceau, T. Hilditch, M. Yongjun Tan, A systematic study on the influence of electrochemical charging conditions on the hydrogen embrittlement behaviour of a pipeline steel, Int. J. Hydrogen Energy 48 (2023) 16501–16516.
[41] P. Pedeferri, Corrosion Science and Engineering, first ed., Springer, 2018.
[42] Y. Chen, Y. Li, C. Chen, Studying the effect of electrode material and magnetic field on hydrogen production efficiency. Studying the effect of electrode material and magnetic field on hydrogen production efficiency, Magnetochem. 8 (2022) 53.
[43] A. Turnbull, 4 - hydrogen diffusion and trapping in metals, in: Richard P. Gangloff, Brian P. Somerday (Eds.), Woodhead Publishing Series in Metals and Surface Engineering, Gaseous Hydrogen Embrittlement of Materials in Energy Technologies, vol. 1, Woodhead Publishing, 2012, pp. 89–128, https://doi.org/10.1533/9780857095374.1.89. ISBN 9780857095367.
[44] M.A. Mohtadi-Bonab, M. Eskandari, K.M.M. Rahman, R. Ouellet, Szpunar. An extensive study of hydrogen-induced cracking susceptibility in an API X60 sour service pipeline steel, Int. J. Hydrogen Energy 41 (2016) 4185–4197, https://doi.org/10.1016/j.ijhydene.2016.01.031.
[45] R. Wang, Effects of hydrogen on the fracture toughness of a X70 pipeline steel, Corros. Sci. 51 (2009) 2803–2810.
[46] M. Cauwels, R. Depraetere, W. De Waele, S. Hertelè, T. Depover, K. Verbeken, Influence of electrochemical hydrogenation parameters on microstructures prone to hydrogen-induced cracking, J. Nat. Gas Sci. Eng. 101 (2022) 104533, https://doi.org/10.1016/j.jngse.2022.104533.
[47] M. Elboujdaini, R.W. Revie, Metallurgical factors in stress corrosion cracking (SCC) and hydrogen-induced cracking (HIC), J. Solid State Electrochem. 13 (2009) 1091–1099, https://doi.org/10.1007/s10008-009-0799-0.
[48] E. Ohaeri, U. Eduok, J. Szpunar, Hydrogen related degradation in pipeline steel: a review, Int. J. Hydrogen Energy 43 (2018) 14584–14617, https://doi.org/10.1016/j.ijhydene.2018.06.064.
[49] Weeks TS, Read DT. Comparison of J-integral from single specimen SE(T) tests on API-5L X100 line pipe steel. In ISOPE 2015 Conference (pp. 1-6). Kona, HI.
[50] Pussegoda LN, Tiku S, Park D, Tyson WR, Gianetto J. J-resistance results from multi-specimen and single-specimen surface notched SEN(T) geometry. In Proceedings of the 2012 9th International Pipeline Conference (Vol. vol. 3: Materials and Joining, pp. 539-544). Calgary, Alberta, Canada: ASME. doi: 10.1115/IPC2012-90565.
[51] Tyson WR, Gianetto JA, Low-Constraint toughness testing: results of a round robin on a draft SE(T) test procedure," Proceedings of the ASME Pressure Vessels & Piping Division Conference (PVP2013), Paris, France, Paper PVP2013-97299.
[52] H.P. Kyriakopoulou, P. Karmiris-Obratański, A.S. Tazedakis, N.M. Daniolos, E. C. Dourdounis, D.E. Manolakos, D. Pantelis, Investigation of hydrogen embrittlement susceptibility and fracture toughness drop after in situ hydrogen cathodic charging for an X65 pipeline steel, Micromachines 11 (2020) 430, https://doi.org/10.3390/mi11040430.
[53] Y. Xing, Z. Yang, X. Yao, X. Wang, M. Lu, L. Zhang, L. Qiao, Effects of hydrogen on the fracture toughness of X80 steel base metal and girth weld under strong cathodic current with in-situ hydrogen charging, Eng. Fail. Anal. 135 (2022) 106143, https://doi.org/10.1016/j.engfailanal.2022.106143.
[54] C. San Marchi, B. Somerday, SANDIA REPORT Technical Reference for Hydrogen Compatibility of Materials Technical Reference for Hydrogen Compatibility of Materials, 2023.
[55] Y. Du, L. Lv, K. Chen, G. Dang, H. Xu, S. Zheng, Investigating variations in hydrogen-assisted crack propagation of X52 pipeline steel with different microstructural characteristics, Corros. Sci. 239 (2024) 112417.
[56] T.T. Nguyen, H.M. Heo, J. Park, S.H. Nahm, U.B. Beak, Fracture properties and fatigue life assessment of API X70 pipeline steel under the effect of an environment containing hydrogen, J. Mech. Sci. Technol. 35 (4) (2021) 1445–1455.
[57] G. Gutierrez-Solana, M. Elices, HIGH-PRESSURE Hydrogen Behavior of a Pipeline Steel, 1982.
[58] E.S. Drexler, R.L. Amaro, A.J. Slifka, P.E. Bradley, D.S. Lauria, Operating hydrogen gas transmission pipelines at pressures above 21 MPa, ASME. J. Pressure Vessel Technol. 140 (6) (2018) 061702, https://doi.org/10.1115/1.4041689.